

Contactless Electromagnetic Phase-Shift Flowmeter for Liquid Metals

Jānis Priede¹, Dominique Buchenau² and Gunter Gerbeth²

¹Applied Mathematics Research Centre, Coventry University, United Kingdom

²Forschungszentrum Dresden-Rossendorf, MHD Department, Germany

E-mail: j.priede@coventry.ac.uk

Abstract. We present a concept and test results of an induction flowmeter for liquid metals. The flow rate is determined by applying a weak AC magnetic field to a liquid metal flow and measuring the flow-induced phase disturbance in the external electromagnetic field. The phase disturbance is found to be more robust than that of the amplitude used in conventional AC flowmeters. The basic characteristics of this type of flowmeter are analysed using simple theoretical models where the flow is approximated by a solid body motion. Design of such a flowmeter is presented and its test results reported.

Keywords: Electromagnetic flowmeter, liquid metal, ac magnetic field

PACS numbers: 41.20.Gz, 47.60.Dx, 47.65.-d, 47.80.Cb

Submitted to: *Meas. Sci. Technol.*

1. Introduction

Accurate and reliable flow rate measurements are required in many technological processes using liquid metals. Commercially available electromagnetic flowmeters typically use electrodes in direct contact to the liquid to measure the voltage induced by the flow in DC magnetic field [1, 2, 3, 4]. Electrodes are not usable in aggressive media like molten metals which require contactless treatment. A well-known example of such a contactless flowmeter is the magnetic flywheel, which is described in the textbook of Shercliff [1] and employed by Bucenieks [5, 6] for flow rate measurements. Such kind of flowmeters have recently been reembodyed under the name of Lorentz force velocimetry [7, 8]. As the name suggests, the Lorentz force sensors measure the electromagnetic force exerted by the flow on a closely placed permanent magnet. This force is proportional to the product of the electrical conductivity of the fluid and the square of the applied magnetic field strength. Another type of flowmeter using a single rotating magnet has recently been reported in [9]. This sensor is based on the equilibrium of the electromagnetic torques caused by the flow on the magnet and by the magnet on the flow. The equilibrium rotation rate is, in a reasonable range of parameters, independent of the strength of the permanent magnet as well as the conductivity of the liquid that makes the measurements insensitive to temperature variations in the liquid.

Alternatively, the flow of liquid metal can be determined in a contactless way by measuring the flow-induced perturbation of an externally applied magnetic field as done, for example, in the so-called flow tomography [10]. The main problem of this method is to measure a weak induced magnetic field with relative amplitude of the order of magnitude of the magnetic Reynolds number $Rm \sim 10^{-4} - 10^{-1}$ on the background of the applied magnetic field. This approach can further be refined by use of AC magnetic field instead of DC one that enables contactless measurements of the electric field induced by the AC magnetic field [11]. There are a number of measurement schemes known which rely on the geometrical compensation of the applied field by a proper arrangement of sending and receiving coils so that only the signal induced by the flow is measured [12, 13]. Such flowmeters employ the flow-induced asymmetry of the magnetic field. Unfortunately, there are a number of side effects such as, for example, the thermal expansion, which can also cause some asymmetry between the receiving coils.

As the flow can disturb not only the amplitude of an AC magnetic field but also its phase distribution, the latter also can be used for the flow rate measurements [14, 15]. In this paper, we analyse the basic characteristics of such a phase-shift flowmeter, present its technical implementation and report the test results. The paper is organised as follows. The basic physical effects are considered in Section 2 using a simple model where the liquid flow is approximated by a solid body motion. In Section 3 we describe the realisation of the phase-shift sensor and present flow rate measurements at two different liquid metal loops. The paper is concluded by a summary in Section 4.

2. Mathematical model

2.1. Basic equations

Consider a medium of electrical conductivity σ moving with velocity $\mathbf{v} = V\mathbf{e}_x$ in an AC magnetic field with the induction \mathbf{B} alternating harmonically with the angular frequency ω . The induced electric field follows from the Maxwell-Faraday equation as $\mathbf{E} = -\nabla\Phi - \partial_t\mathbf{A}$, where Φ is the electric potential, \mathbf{A} is the vector potential and $\mathbf{B} = \nabla \times \mathbf{A}$. The density of the electric current induced in the moving medium is given by Ohm's law

$$\mathbf{j} = \sigma(\mathbf{E} + \mathbf{v} \times \mathbf{B}) = \sigma(-\nabla\Phi - \partial_t\mathbf{A} + \mathbf{v} \times \nabla \times \mathbf{A}).$$

Assuming the AC frequency to be sufficiently low to neglect the displacement current, Ampere's law $\mathbf{j} = \frac{1}{\mu_0}\nabla \times \mathbf{B}$ leads to the following advection-diffusion equation for the vector potential

$$\partial_t\mathbf{A} + (\mathbf{v} \cdot \nabla)\mathbf{A} = \frac{1}{\mu_0\sigma}\nabla^2\mathbf{A}, \quad (1)$$

where the gauge invariance of \mathbf{A} has been used to specify the scalar potential as $\Phi = \mathbf{v} \cdot \mathbf{A} - \frac{1}{\mu_0\sigma}\nabla \cdot \mathbf{A}$. In the following, we consider an applied magnetic field varying in time harmonically as $\mathbf{A}_0(\mathbf{r}, t) = \mathbf{A}_0(\mathbf{r})\cos(\omega t)$ that allows us to search for a solution in the complex form $\mathbf{A}(\mathbf{r}, t) = \Re[\mathbf{A}(\mathbf{r})e^{i\omega t}]$. Then (1) for the amplitude distribution of the vector potential takes the form

$$i\omega\mathbf{A} + (\mathbf{v} \cdot \nabla)\mathbf{A} = \frac{1}{\mu_0\sigma}\nabla^2\mathbf{A}. \quad (2)$$

Further we focus on a simple 2D externally applied magnetic field which is invariant along the direction of unit vector $\boldsymbol{\varepsilon}$. Such a magnetic field can be specified by a single component of the vector potential $\mathbf{A} = \boldsymbol{\varepsilon}A$ as $\mathbf{B} = \nabla \times \boldsymbol{\varepsilon}A = -\boldsymbol{\varepsilon} \times \nabla A$, where \mathbf{B} has only two components in the plane perpendicular to $\boldsymbol{\varepsilon}$. The continuity of \mathbf{B} at the interface S between conducting and insulating media imply the following boundary conditions:

$$[A]_S = [\partial_n A]_S = 0, \quad (3)$$

where $[f]_S$ denotes the jump of quantity f across the boundary S ; $\partial_n \equiv (\mathbf{n} \cdot \nabla)$ is the derivative normal to the boundary.

2.2. Solution for a conducting layer

We start with a simple model where the conducting medium is a layer of thickness $2H$, and the applied magnetic field is a harmonic standing wave with the vector potential amplitude given by

$$\mathbf{A}_0(\mathbf{r}, t) = \mathbf{e}_z A_0(\mathbf{r}, t) = \mathbf{e}_z \hat{A}_0(y) \cos(kx) \cos(\omega t),$$

where k is the wavenumber in the x -direction, as shown in figure 1(a). Henceforth, we choose the half-thickness H as the length scale and introduce a dimensionless AC frequency $\bar{\omega} = \mu_0\sigma\omega H^2$ and the magnetic Reynolds number as $Rm = \mu_0\sigma V H$, where the latter represents

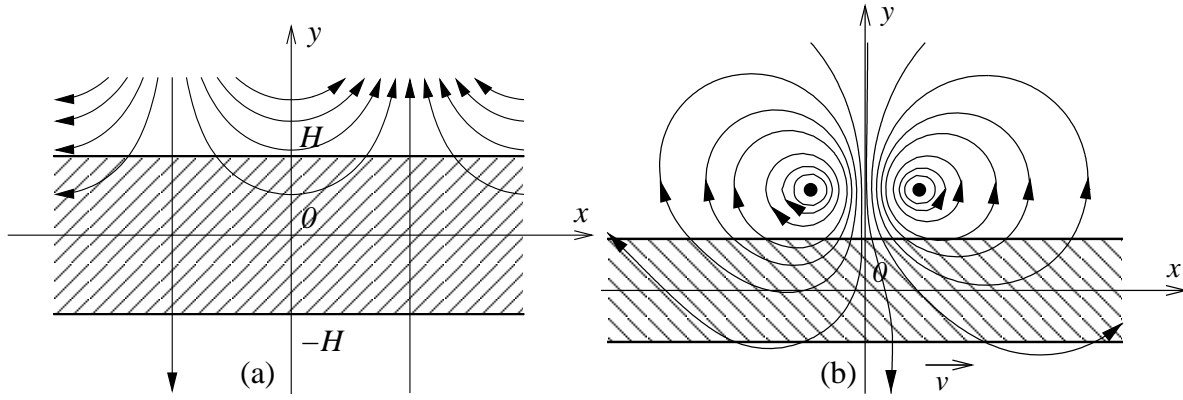


Figure 1. Model of conducting layer of thickness $2H$ in an external magnetic field represented by a standing harmonic wave (a) and generated by a couple of straight wires (b).

the dimensionless velocity of the medium. Although for typical liquid metal flows $Rm \ll 1$, the following analysis will not be limited to this case unless stated otherwise. For free space with $\sigma = 0$, equation (2) takes the form

$$\frac{d^2 \hat{A}_0}{dy^2} - k^2 \hat{A}_0 = 0 \quad (4)$$

and has the solution

$$\hat{A}_0(y) = C_0 e^{k(y-1)}, \quad (5)$$

where the constant C_0 defines the amplitude of the applied magnetic field. Further, it is important to notice that the applied magnetic field, which is assumed in the form of a standing wave, can be represented as a superposition of two oppositely travelling waves $A_0(\mathbf{r}, t) = \frac{1}{2} [A_0^+(\mathbf{r}, t) + A_0^-(\mathbf{r}, t)]$, where $A_0^\pm(\mathbf{r}, t) = \hat{A}_0(y) \cos(\omega t \pm kx)$. This implies that the solution for the vector potential can also be sought in a similar complex form as $A(\mathbf{r}, t) = \frac{1}{2} [A^+(\mathbf{r}, t) + A^-(\mathbf{r}, t)]$, where $A^\pm(\mathbf{r}, t) = \Re [\hat{A}^\pm(y) e^{i(\omega t \pm kx)}]$ are oppositely travelling fields. The solution for these oppositely travelling fields, which is governed by equation (4) in the free space above the layer ($y \geq 1$), can be represented as $\hat{A}^\pm(y) = \hat{A}_0(y) + \hat{A}_1^\pm(y)$, where $\hat{A}_1^\pm(y) = C_1^\pm e^{-k(y-1)}$ is the induced field. In the free space below the layer at $y \leq -1$, the solution satisfying (4) is obtained as $\hat{A}(y) = C_3^\pm e^{k(y+1)}$. In the conducting layer defined by $-1 \leq y \leq 1$, equation (2) for both travelling fields takes the form

$$\frac{d^2 \hat{A}^\pm}{dy^2} - \kappa_\pm^2 \hat{A}^\pm = 0, \quad (6)$$

where $\kappa_\pm = \sqrt{k^2 + i(\bar{\omega} \pm kRm)}$, and has the solution which can be written as $\hat{A}(y) = C_2^\pm \sinh(\kappa_\pm y) + D_2^\pm \cosh(\kappa_\pm y)$. The unknown constants following from the boundary conditions (3) are

$$\begin{aligned} C_2^\pm &= C_0 \frac{k}{k \sinh(\kappa_\pm) + \kappa_\pm \cosh(\kappa_\pm)}, & C_1^\pm &= D_2^\pm \cosh(\kappa_\pm) + C_2^\pm \sinh(\kappa_\pm) - C_0, \\ D_2^\pm &= C_0 \frac{k}{k \cosh(\kappa_\pm) + \kappa_\pm \sinh(\kappa_\pm)}, & C_3^\pm &= D_2^\pm \cosh(\kappa_\pm) - C_2^\pm \sinh(\kappa_\pm). \end{aligned} \quad (7)$$

This solution can easily be extended to the external magnetic field generated by a finite-size coil. The simplest model of such a coil consists of two parallel straight wires fed with an AC current of amplitude I_0 flowing in opposite directions along the z -axis at distance $2s$ in the x -direction and placed at height h above the upper surface of the layer, as shown in figure 1(b). The free-space distribution of the vector potential amplitude having only a z -component, which is further scaled by $\mu_0 I_0$, is governed by

$$\nabla^2 A_0 = -\delta(\mathbf{r} - s\mathbf{e}_x) + \delta(\mathbf{r} + s\mathbf{e}_x), \quad (8)$$

where $\delta(\mathbf{r})$ is the Dirac delta function and \mathbf{r} is the radius vector from the midpoint between the wires. The problem is solved by the Fourier transform $\hat{A}(y; k) = \int_{-\infty}^{\infty} A(x, y) e^{ikx} dx$ that transforms (8) into

$$\frac{d^2 \hat{A}_0}{dy^2} - k^2 \hat{A}_0 = -f_k \delta(y), \quad (9)$$

where $f_k = \int_{-\infty}^{\infty} [\delta(x - s) - \delta(x + s)] e^{ikx} dx = 2i \sin(ks)$. The solution of (9) decaying at $y \rightarrow \pm\infty$ can be written as $\hat{A}_0(y; k) = c_k e^{-|ky|}$, where the unknown coefficient

$$c_k = \frac{f_k}{2|k|} = \frac{i \sin(ks)}{|k|}. \quad (10)$$

is found from the boundary condition $[d\hat{A}/dy]_{y=0} = -f_k$, which follows from (9). The solution for each mode specified by wavenumber k is obtained by replacing C_0 in (5) and (7) by c_k from (10). The final solution is obtained by the inverse Fourier transform $A(x, y) = \frac{1}{2\pi} \int_{-\infty}^{\infty} \hat{A}(x; k) e^{-ikx} dk$, which can efficiently be calculated the Fast Fourier Transform (FFT).

2.3. Numerical results

For the physical interpretation of the following results note that the magnetic flux through a surface is given by the circulation of the vector potential along the contour encircling that surface. For the simple 2D case under consideration, when the vector potential has only one component, the difference of the vector potential between two points defines the linear flux density between two lines parallel to the vector potential at those two points. The same holds also for the time derivative of the corresponding quantities. Thus, the difference of the vector potential amplitudes between two points is proportional to the e.m.f. amplitude which could be measured by an idealised coil consisting of two straight parallel wires placed along the z -axis at these points. Correspondingly, the single-point vector potential considered below gives the e.m.f. measured by a ‘wide’ coil with the second wire placed sufficiently far away in the region of a negligible magnetic field.

Spatially-harmonic magnetic field The flux lines and the corresponding phase distribution of the vector potential are plotted in figure 2 for the layer at rest (*a, c, e*) and moving to the right with $Rm = 1$ (*b, d, f*). The flux components in the phase and shifted by $\pi/2$ relative to the applied magnetic field correspond to the time instants when the applied field is at

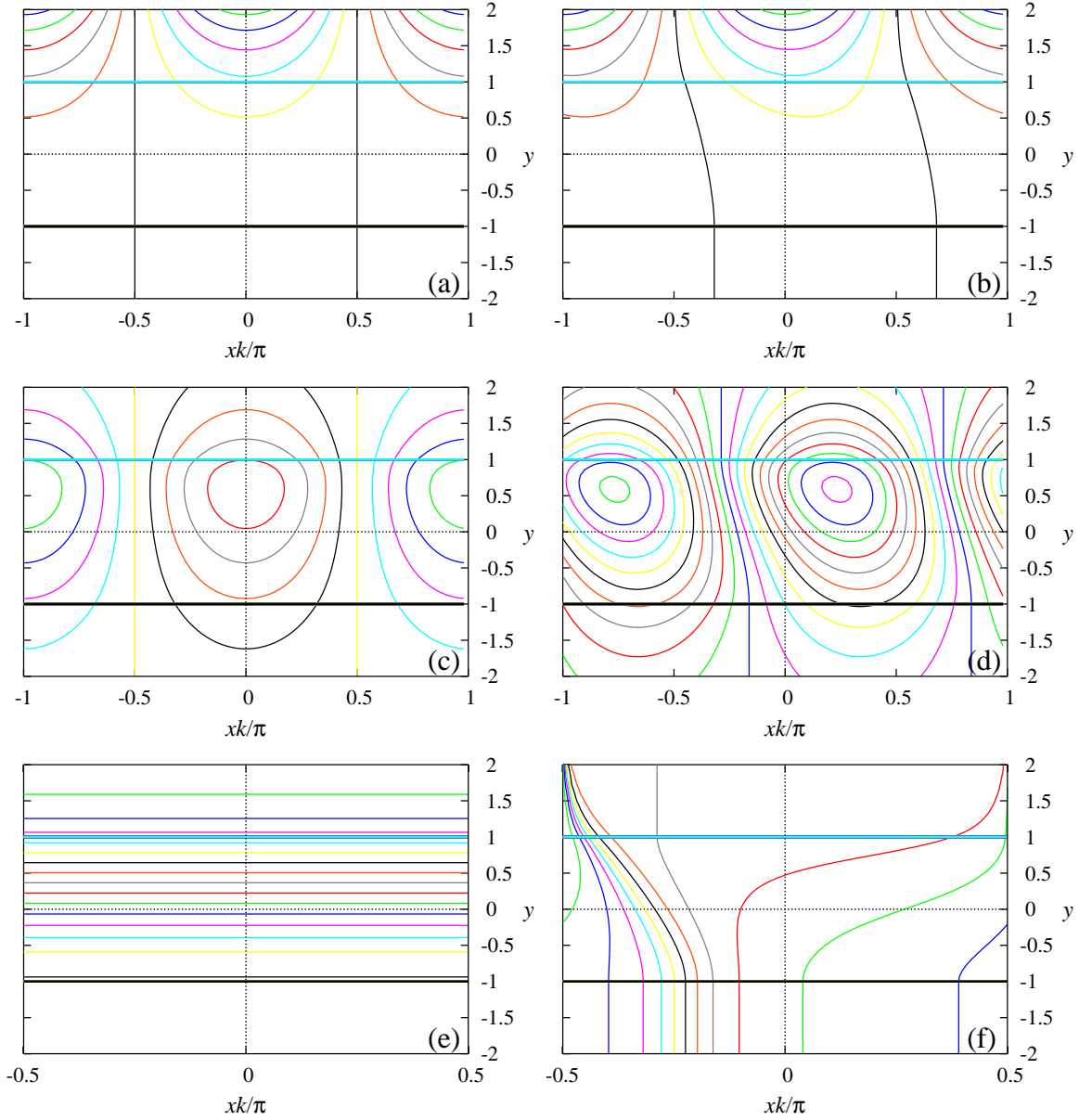


Figure 2. The magnetic flux components in the phase with the applied field (a,b), shifted by $\pi/2$ (c,d), and the corresponding phase distribution (e,f) for $\bar{\omega} = 1$ and $k = 1$ at $Rm = 0$ (layer at rest) (a,c,e) and $Rm = 1$ (b,d,f).

maximum and absent, respectively. In the latter case, the magnetic field is entirely due to the eddy currents. Figure 2(e) shows that for the layer at rest, the phase is constant over half-wavelength of the applied field and varies only with the vertical position except below the layer, where the phase does not vary at all. It is important to note that this phase distribution is actually piece-wise constant with the phase jumping by π across the nodes of the standing wave. This phase discontinuity, which is important for the subsequent analysis, is due to the two adjacent halves of standing wave oscillating in opposite phases. As seen in figure 2(f), this simple phase distribution vanishes as soon as the layer starts to move. Although for a

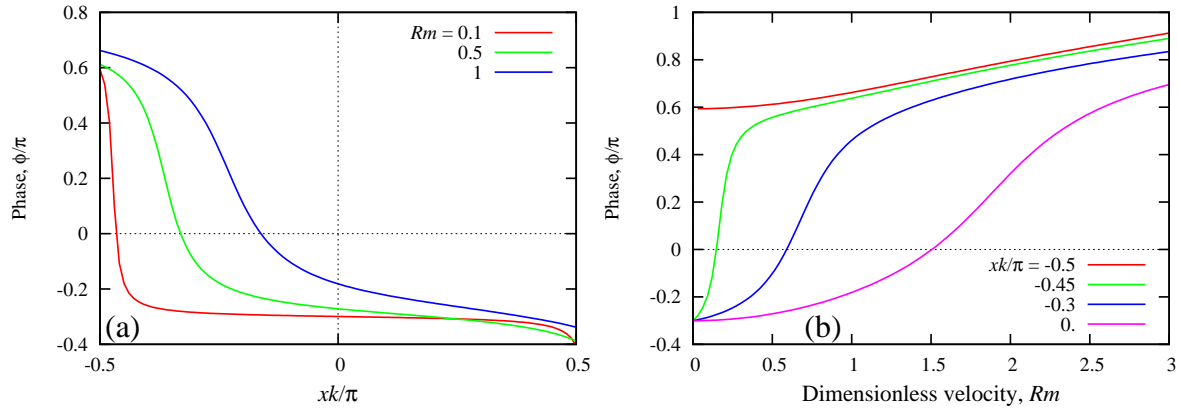


Figure 3. Phase distribution over a half-wavelength of the applied magnetic field at various velocities defined by Rm (a) and the phase variation with the velocity at different points along the bottom of the layer for $\bar{\omega} = 1$ and $k = 1$.

moving layer the phase is no longer horizontally constant, it is still vertically constant below the layer, where the field itself decays exponentially with the vertical distance. This is an important result which illustrates why the phase measurements, in contrast to those of the amplitude, are more robust and, in this case, actually independent of the vertical position of the receiving coils. Note that such a perfect vertical phase homogeneity holds only when the applied magnetic field is a standing harmonic wave.

Figure 3(a) shows the phase distribution along the bottom of the layer over a half-wavelength between two nodes of the applied field for various dimensionless velocities Rm . Note that henceforth the phase ϕ is presented in radians and scaled by π so that $\pm\pi$ phase corresponds to $\phi = \pm 1$. The original phase discontinuity between adjacent half-waves shows up in 3(a) as soon as the layer starts to move. The increase in the velocity is seen to smooth out this discontinuity and to shift it further downstream. Note that the total phase variation over half-wave remains ± 1 ($\pm\pi$) regardless of the velocity, as it should be for a spatially-periodic solution.

The phase variation with the velocity at several observation points at the bottom of the layer is plotted in figure 3(b). As seen, the closer the observation point to the node, the steeper the phase variation, but the shorter the velocity range of this variation. The steep part of the phase variation with the velocity is obviously due to the observation point laying in the transition region between two adjacent half-waves discussed above. The phase variation is relatively weak when the observation point occurs before or after the transition region. The latter requires significant velocities with $Rm \gtrsim 1$. This illustrates the importance of the location of observation point which for low velocities should be placed downstream in close vicinity to the node or symmetry plane of the applied magnetic field, where the phase varies significantly with the velocity. In the case of the phase difference measured between two coils, the measurement sensitivity can be increased by a horizontal offset of the sensing coils with respect to the exciting coil so that one of the sensing coils gets close to the midplane, as demonstrated experimentally in the following.

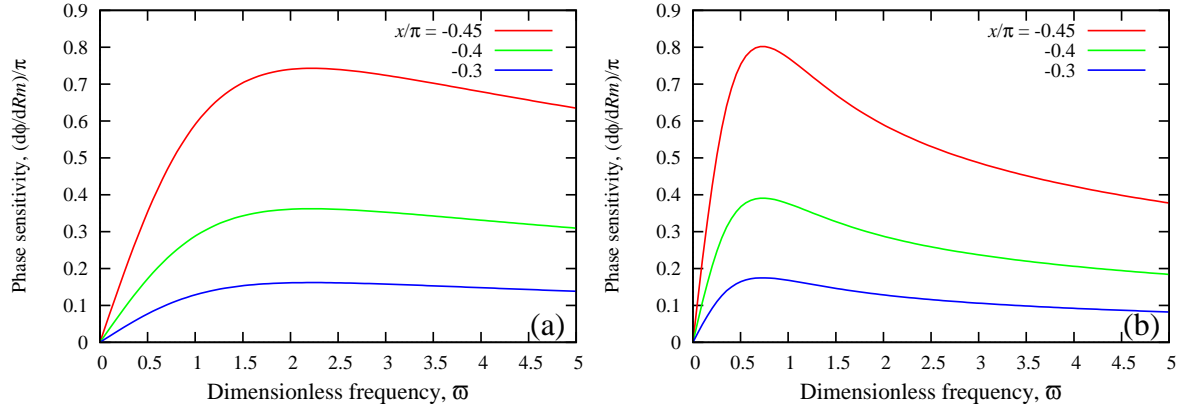


Figure 4. The phase sensitivity versus the dimensionless frequency $\bar{\omega}$ at various horizontal observation positions below the layer for $k = 1$ (a) and $k = 0.5$ (b).

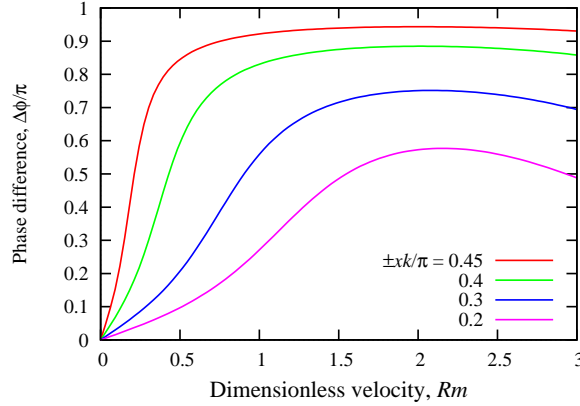


Figure 5. Phase difference between two observation points placed symmetrically with respect to $x = 0$ below the layer versus the dimensionless velocity Rm for $\bar{\omega} = 2$ and $k = 1$.

To determine the optimal frequency of the applied AC field it is useful to consider the rate of variation of phase φ with the velocity Rm . For sufficiently small Rm , which presents the main interest here, this phase sensitivity is defined by $\left. \frac{d\varphi}{dRm} \right|_{Rm=0}$. The phase sensitivity plotted in figure 4 versus the dimensionless frequency $\bar{\omega}$ shows that there is an optimal AC frequency $\bar{\omega}_o$ at which the sensitivity attains a maximum. This optimal frequency, which is seen to be independent of the horizontal position of the observation point along the bottom of the layer, decreases with the wavenumber of the applied magnetic field: $\bar{\omega}_o \approx 2.1$ for $k = 1$ and $\bar{\omega}_o \approx 0.73$ for $k = 0.5$.

The phase difference between two observation points placed symmetrically at various distances from $x = 0$ below the layer is plotted in figure 5 versus Rm for $\bar{\omega} = 2$ and $k = 1$. As discussed above, the velocity sensitivity of this phase difference is seen to increase as the observation points are moved closer to the nodes at $x = \pm 0.5$. As already noted above, the closer the observation points to the node, the higher the sensitivity but the shorter the velocity range which can be measured. The last is because the phase difference is seen first to saturate and then to reduce on the account of smoothing by the moving medium. This limits

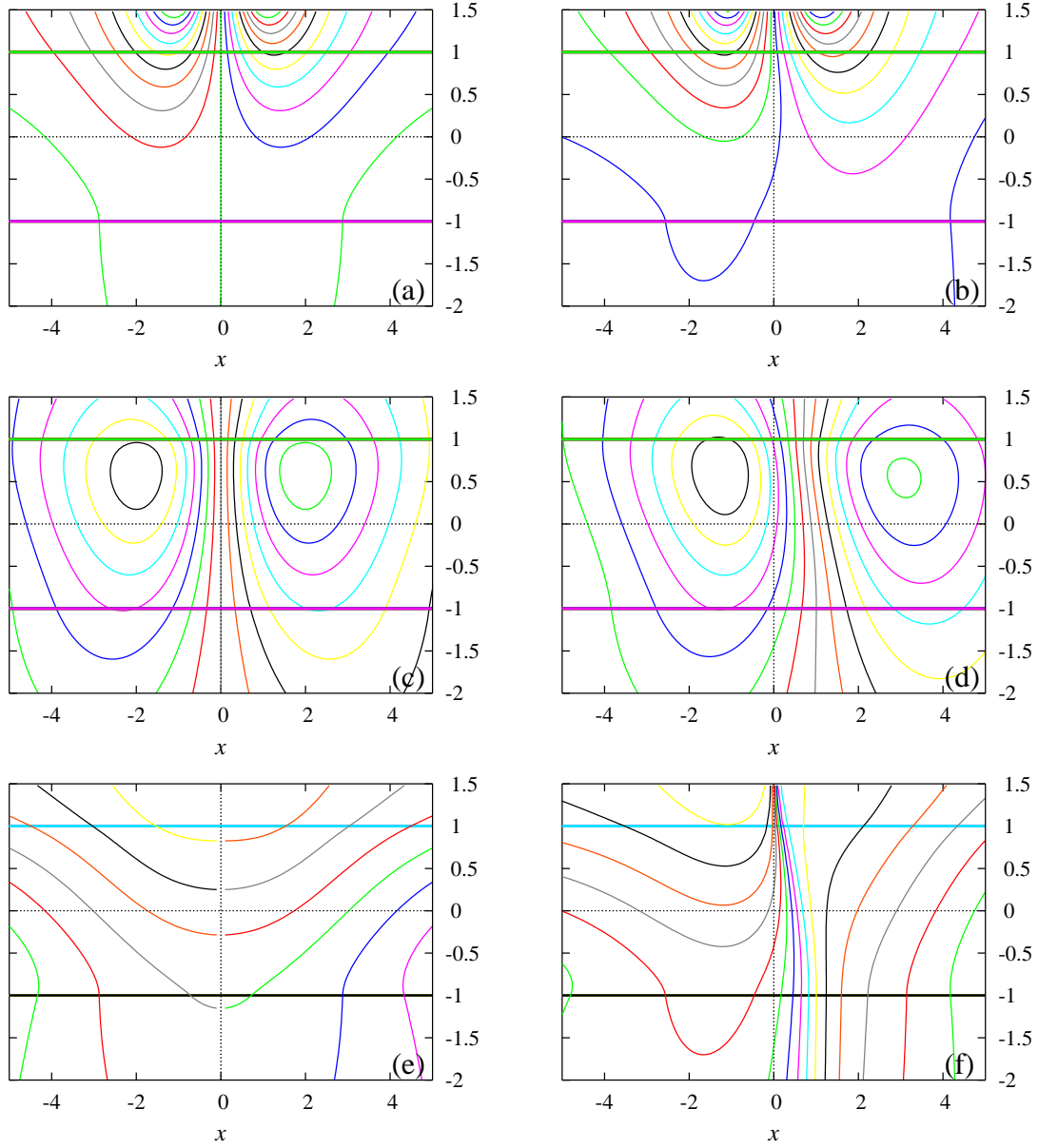


Figure 6. The flux components in the phase with the applied field (a,b), shifted by $\pi/2$ (c,d), and the corresponding phase distribution (e,f) for the external magnetic field generated by two parallel wires with $\bar{\omega} = 1$ at $Rm = 0$ (layer at rest) (a,c,e) and $Rm = 1$ (b,d,f).

the maximum velocity which can be measured, but the smoothing effect becomes significant only at $Rm \gtrsim 2$, which corresponds to rather high velocities in reality.

Sending coil modelled by two straight wires In this section, we turn to a more complicated external magnetic field generated by a couple of parallel wires with opposite currents separated the horizontal distance $2s = 2$ and put at the height $h = 1$ above the layer. The flux lines and the corresponding phase distribution of the vector potential are plotted in figure 6 for the layer at rest (a,c,e) and moving to the right with $Rm = 1$ (b,d,f). In the first case,

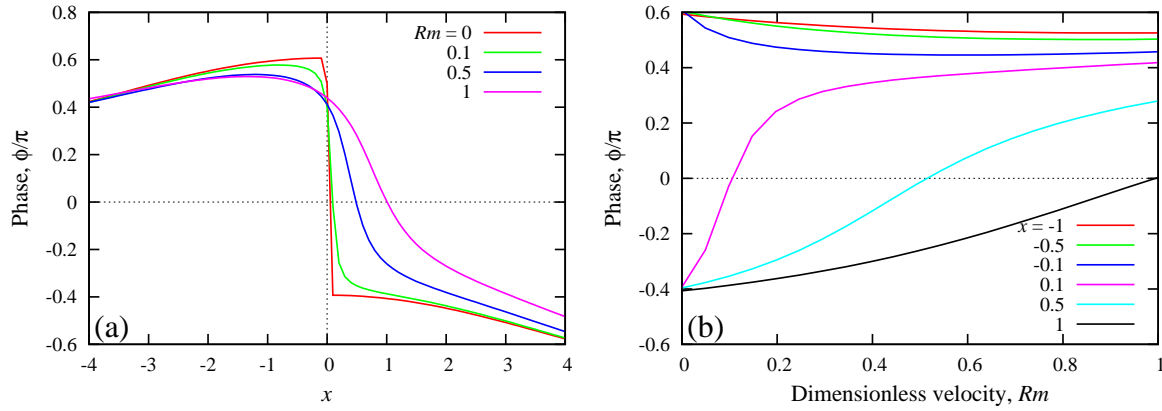


Figure 7. Phase distribution of the vector potential at various velocities defined by Rm (a) and phase variation with the velocity at different points along the bottom of the layer for $\bar{\omega} = 1$ (b).

the vector potential distribution is exactly anti-symmetric with respect to the symmetry plane $x = 0$, which is, thus, analogous the node in a standing wave. Correspondingly, there is a phase jump of π at $x = 0$ when the layer is at rest. Figures 6(b,d,f) show that the motion of the layer brakes the symmetry and smooths out the phase discontinuity. Although, as seen in 6(f), the phase distribution below the layer is no more vertically invariant as for the spatially-harmonic external magnetic field considered above, its vertical variation is still weak in comparison to that of the amplitude.

Figure 7 shows the phase distributions at various velocities (Rm) (a), and the phase variation with Rm at different points along the bottom of the layer for $\bar{\omega} = 1$. In contrast to the spatially-harmonic external magnetic field, now the phase distribution is slightly uniform rather than piece-wise constant along the layer even when the latter is at rest. Nevertheless, the field distribution is still symmetric with respect to the midplane between the wires. The motion is seen to break this symmetry and to smooth out the phase jump at the midplane. The phase variation with the velocity is shown in figure 7(b) at several points along the bottom of the layer for $\bar{\omega} = 1$. It is important to note that sufficiently close to the symmetry plane, the original phase non-uniformity at $Rm = 0$ is small relative to that induced by the motion.

The phase sensitivity, introduced in the previous section, which is plotted in figure 8(a) versus the dimensionless frequency shows that the optimal frequency at which the phase sensitivity attains a maximum for this model is $\bar{\omega} \approx 0.14$. This frequency is relatively low because, in accordance to (10), the applied magnetic field is dominated by low-wavenumber modes. The reduction of the sensitivity above the optimal frequency is rather slow in comparison to its steep increase at sub-optimal frequencies. Thus, the loss of sensitivity at $\bar{\omega} \approx 1$ is not very significant, especially for the observation points further away from the midplane. The phase difference between the pairs of observation points placed symmetrically with respect to the midplane, which is plotted in figure 8(b) for $\bar{\omega} = 1$, shows the same tendency as for the spatially harmonic external field. Namely, the closer the observation points to the midpoint, the higher the sensitivity but the faster the saturation of the phase difference.

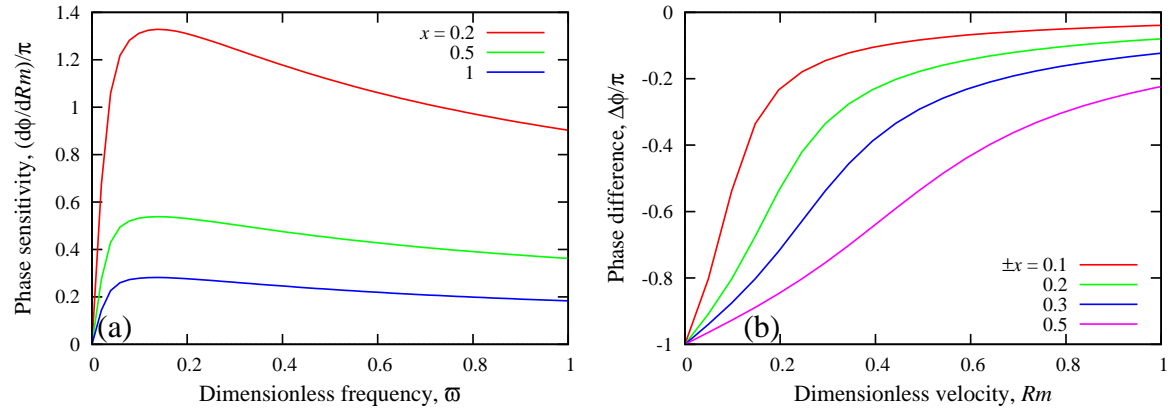


Figure 8. The phase sensitivity versus the frequency at various horizontal observation positions at the bottom of the layer (a) and the phase difference between two observation points placed symmetrically with respect to $x = 0$ at the bottom of the layer versus the dimensionless velocity Rm for $\bar{\omega} = 1$ (b).

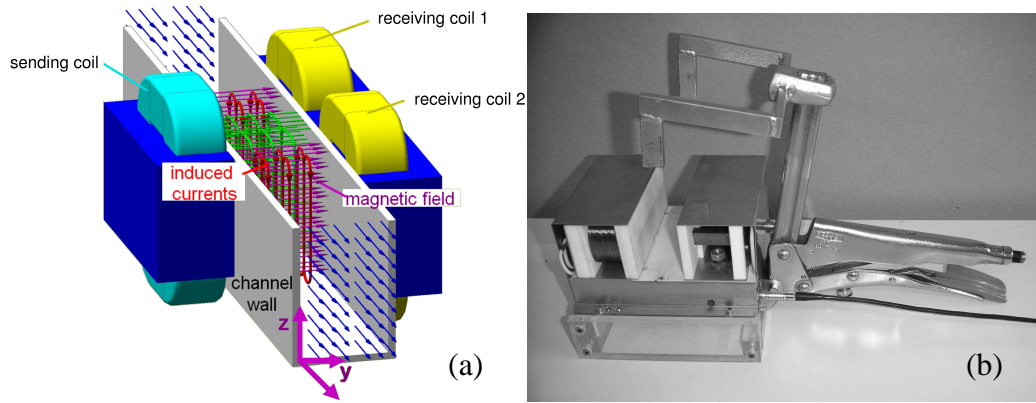


Figure 9. Experimental concept (a) and laboratory model (b) of the phase-shift flowmeter.

Thus, the choice of the observation points depends on the range of velocities which is to be measured. In this case, when the observation points are placed exactly symmetrically with respect to the midpoint, the original phase difference at $Rm = 0$ is π . This difference reduces and tends to zero with the increase of Rm as the phase is smoothed out by the advection of the magnetic field.

3. Flowmeter realisation and test results

A realisation of the flowmeter based on the described principles is shown in figure 9. It consists of a sending coil and two receiver coils placed on the opposite side of the duct. This phase-shift flowmeter [14, 15] operates like a split transformer with two secondary coils. The sending coil generates an AC magnetic field across the channel carrying the liquid metal flow. The phase shift between the voltages induced in the two receiver coils is the main quantity measured.

Generally, we distinguish between two possible arrangements of the flowmeter – a

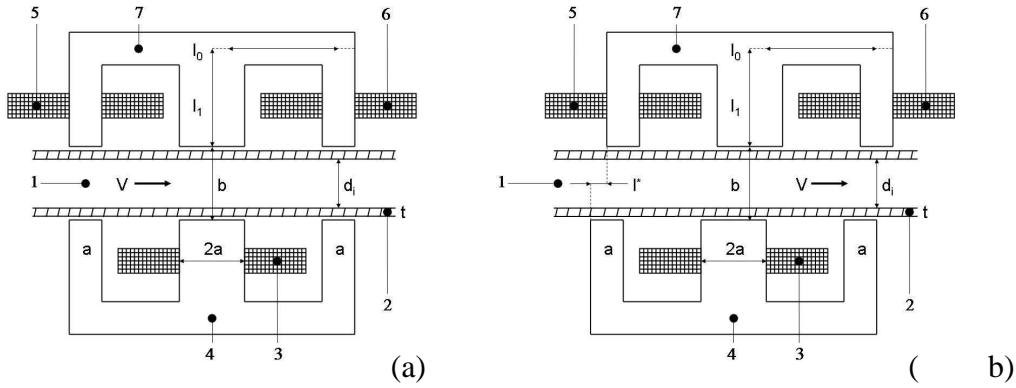


Figure 10. Setup of the contactless flowmeter in the symmetric (a) and asymmetric (b) arrangement with: 1 - channel, 2 - channel-wall, 3 - sending-coil, 4 and 7 - laminated mild-iron, 5 and 6 - receiving coils, V - averaged flow rate in the channel, $d_i = 2H_i$ - inner diameter of the channel, and l^* - displacement length.

symmetric and an asymmetric one, where the receiver coils are shifted by the displacement length l^* with respect to the sending coil in order to increase the sensitivity of the flowmeter as suggested by the theoretical analysis above. Both arrangements are shown in figure 10.

3.1. Test facilities

The GaInSn test facility is designed to operate with a metallic melt at room temperature of high electrical conductivity ($\sigma = 3.3 \times 10^6 S/m$). The melt is driven by a permanent magnet induction pump [16] with an adjustable flow rate. The lower part of the loop basically consists of circular stainless steel tubes with inner diameter of 27 mm and a wall thickness of 2.6 mm. The upper part of the loop consists of three independent test sections with a length of 400 mm each. All three test sections have the same inner diameter and wall thickness. The test sections can be opened and closed independently of each other by valves. During experiments two test sections were closed in order to have a maximum mean flow velocity of $V = 1.4 m/s$ in the third test section used. This maximum melt velocity corresponds to $Rm = 0.08$ with the pipe radius taken as the length scale H . All test sections were kept completely filled with the melt. The flow rate was independently controlled by a commercial flowmeter with an electrical contact to the melt, the operation of which was additionally verified by Ultrasonic Doppler Velocimetry measurements of the local flow field [17]. The commercial flow rate sensor was additionally used to ensure an automatic control of the flow rate in order to compensate for the drop of the electrical conductivity of the melt caused by its heating by the pump.

Further experiments were carried out at the sodium-loop [18]. Pipes and ducts were made of stainless steel ($\sigma_w = 1.3 \times 10^6 S/m$) with the cross-section of $45 \times 45 mm^2$ in a horizontal and $45 \times 40 mm^2$ in a vertical test section, which could be separated from each other by valves. Sodium has a high electrical conductivity of $\sigma = 9 \times 10^6 S/m$ at the operation temperature of 170°C. The flow was driven by an electromagnetic linear pump which provided a maximum velocity of 1.5 m/s in the ducts of the loop corresponding to a maximum flow rate of 3 l/s. This maximum melt velocity corresponds to $Rm = 0.4$ with the duct half-width of 22.5 mm

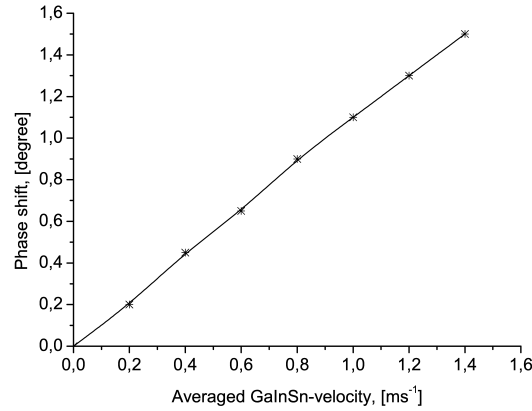


Figure 11. Measured phase shift at the GaInSn loop depending on the flow rate in the symmetrically adjusted case (emitter frequency 600 Hz).

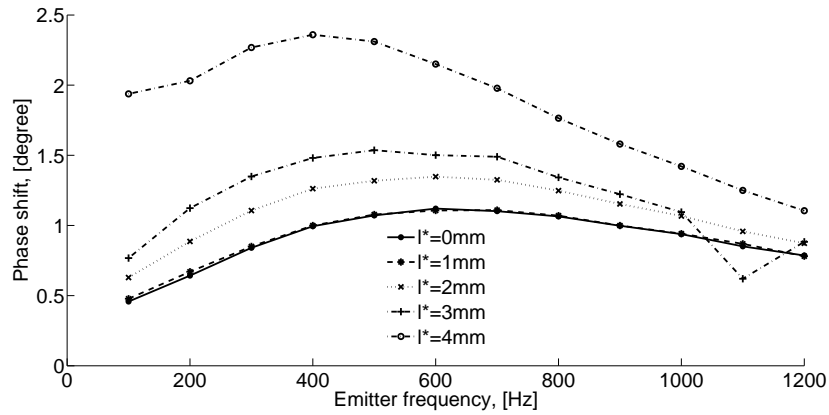


Figure 12. Frequency responses measured at the GaInSn loop for insulating pipe walls and different sensor adjustments at an averaged melt velocity of 1 m/s .

taken as the length scale.

3.2. Flow rate measurements

Flow rate measurements at the GaInSn loop Figure 11 shows the phase shift at the GaInSn loop depending on the mean velocity V in a pipe with insulating walls. As seen, the measured phase shifts vary nearly linearly with the flow rate. To determine the frequency producing the highest signal in the symmetric and asymmetric flowmeter arrangements, the frequency responses of the flowmeter were investigated (see figure 12). All experiments were carried out under the same temperature of the melt, flow rate and velocity profile. In the symmetric case, the optimal frequency was about 620 Hz , which decreased down to about 400 Hz when the displacement length was increased to $l^* = 4\text{ mm}$. This optimal frequency of 620 Hz corresponds to $\bar{\omega} = 2.9$.

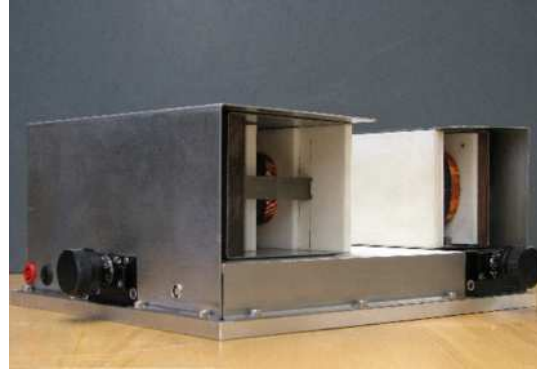


Figure 13. Photograph of the electromagnetic phase-shift flowmeter.

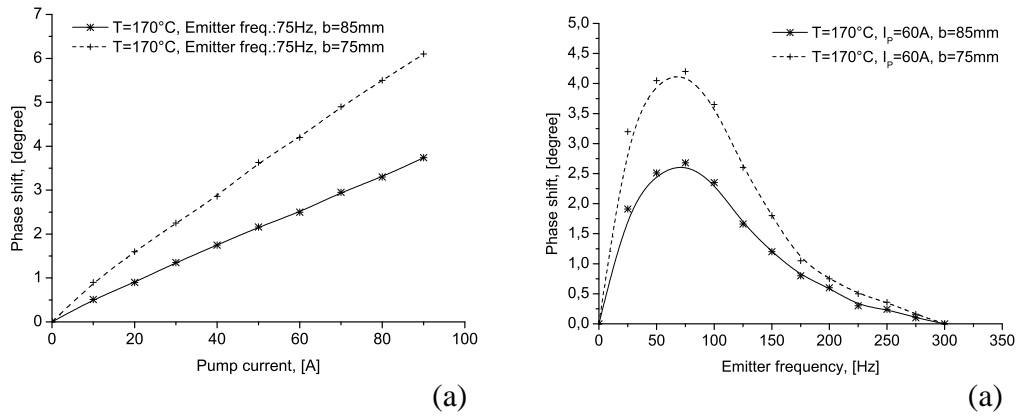


Figure 14. Measurements taken at the sodium loop with a symmetric flowmeter arrangement: (a) frequency response and (b) the phase shift versus the pump current.

Measurements at the sodium loop The applied phase shift flowmeter shown in figure 13 has a sending coil of 500 windings placed on one side of the channel and two receiving coils with 1000 windings each on the opposite side. The sending coil was fed by an alternating current in the range from a few tenths up to 3 A. Both the sending and the receiving coils are furnished with a high-permeability transformer core. The coil wires were coated by two layers of high temperature resistant polyamide ($T = 260^\circ\text{C}$). Furthermore, the coils were encased in the ceramic material MARCOR, which can withstand temperatures up to 800°C and, thus, protects the sending and receiving coils from the hot pipe or channel.

Figure 14 presents the measurements of the frequency response in a symmetric arrangement as a function of the width of the coil gap for a given flow rate and input current of 500mA . The results shown in figure 14(a) indicate that the optimal frequency is about 70Hz which is much lower compared to the GaInSn case due to the higher electrical conductivity and the larger pipe width in the sodium case. This optimal frequency corresponds to $\bar{\omega} = 2.5$. The phase shift measurements seen in figure 14(b) for two different widths of the coil gap show again a very good linearity with the averaged sodium velocity.

4. Summary and conclusions

In this paper, we have presented a conceptual design of a new contactless AC induction flowmeter for liquid metal flows based on the phase shift measurements. This flowmeter employs the fact that the flow of a conducting liquid disturbs not only the amplitude but also the phase distribution of an applied AC magnetic field. In order to figure out the basic physical effects we considered a simple physical model where the liquid flow was approximated by a solid-body motion, and the conducting medium was restricted to a layer of finite thickness. The sender coil was approximated by a spatially-harmonic standing magnetic wave in one case and by a couple of straight wires placed above the layer in another case.

In the case of exciting magnetic field in the form of a standing harmonic wave, the phase has a typical piece-wise constant distribution along the wave with the discontinuities at the wave nodes when there is no flow. These discontinuities are smoothed out as soon as the flow sets in and a strong phase gradient appears in the vicinity of the original wave nodes. This phase variation can be measured to determine the flow velocity. The closer the observation point to the node, the higher the sensitivity of the phase to the velocity but the lower the velocity at which the variation of the phase saturates. Thus, the higher the sensitivity, the lower the maximal velocity which can be measured. There is an optimal AC frequency of the applied magnetic field which ensures maximal sensitivity of the phase with respect to the velocity at small Rm . For the observation points below the layer, the optimal frequency reduces with the increase of the wavelength of the applied magnetic field. In the case of a spatially-harmonic standing magnetic wave, the phase is independent of the vertical distance below the layer.

The phase distribution becomes more complicated when the magnetic field is generated by a coil of finite size which was modelled here by a couple of two straight wires placed parallel to the conducting layer of finite thickness. In this case, the phase is no longer uniform along the layer even without the motion but there is still a characteristic phase jump by 180 degrees at the midplane between the wires while the field itself is symmetric with respect to this plane. Motion of the layer smooths out the discontinuity and breaks the symmetry of the phase distribution with respect to the midplane. The asymmetry of phase distribution caused by the motion can be used to determine its velocity. For this purpose we consider the phase difference between two observation points (receiver coils) placed symmetrically with respect to the midplane. The original phase non-uniformity at $Rm = 0$ becomes relatively small when the observation points are placed sufficiently close to the midplane which is necessary for the detection of small velocities. At higher velocities, the original phase non-uniformity becomes negligible with respect to that induced by the flow. Although the optimal frequency is rather low ($\bar{\omega} \approx 0.14$) for such a coil of finite size, where the exciting magnetic field is dominated by long-wavelength modes, the decrease of sensitivity with frequency is slow that allows one to work at frequencies above the optimum at $\bar{\omega} \approx 1$ without a significant loss of sensitivity. The distance of observation points (receiving coils) from the symmetry plane depends on the velocity range to be measured. A smaller distance ensures a higher sensitivity advantageous for lower velocities but results in a reduced sensitivity at higher velocities because of the

saturation effect.

Based on these ideas a laboratory model of such a flowmeter has been built and tested at a GaInSn and a sodium loop. In both test cases a linear relation between the measured phase-shift and the flow rate in the pipe was obtained. These measurements showed that the phase-shift flowmeter is a robust and accurate measurement technique with high temporal resolution.

Acknowledgments

This work was supported by Deutsche Forschungsgemeinschaft in frame of the Sonderforschungsbereich 609, and by the European Commission under contract FI6W-CT-2004-516520 in frame of the project EUROTRANS.

References

- [1] Shercliff J A 1962 *The Theory of Electromagnetic Flow Measurement* Cambridge University Press: Cambridge
- [2] Bevir M K 1970 The theory of induced voltage electromagnetic flowmeters *J. Fluid Mech.* **43** 577-590
- [3] Engl W L, Arch. für Elektrotechnik 54 (1972) 269-277 (in German)
- [4] Shimizu T, Takeshima N and Jimbo N 2000 A numerical study on Faraday-type electromagnetic flowmeter in liquid metal system *J. Nucl. Sc. Techn.* **37** 1038-1048
- [5] Buceniks I 2002 Electromagnetic induction flowmeter on permanent magnets *Proceedings 5th Int. PAMIR conference on Fundamental and Applied MHD (Ramatuelle, France, September)* 103-105
- [6] Buceniks I 2005 Modelling of rotary inductive electromagnetic flowmeter for liquid metal flow control. *Proceedings 8th Int. Symp. on Magnetic Suspension Technology (Dresden, Germany, September)* 204-208
- [7] Thess A, Votyakov E V and Kolesnikov Y 2006 Lorentz force velocimetry *Phys. Rev. Lett.* **96** 164501
- [8] Thess A, Votyakov E, Knaepen B and Zikanov O 2007 Theory of Lorentz force flowmeter *New J. Physics* **9** 299
- [9] Priede J, Buchenau D and Gerbeth G 2009 Force-free and contactless sensor for electromagnetic flowrate measurements *Magnetohydrodynamics* **45** 451-458
- [10] Stefani F, Gundrum Th and Gerbeth G 2004 Contactless inductive flow tomography *Phys. Rev. E* **70** 056306
- [11] Gundrum Th, Stefani F, Gerbeth G 2006 Experimental aspects of contactless inductive flow tomography *Magnetohydrodynamics* **42** 153-160
- [12] Feng C C, Deeds W E and Dodd C V 1975 Analysis of eddy-current flowmeters *J. Appl. Physics* **46** 2935-2940
- [13] Dementev S, Barbogallo F, Groeschel F, Buceniks I, Krysko S and Poznyaks A 2002 Preliminary LBE test of the electromagnetic flow meter for the MEGAPIE target *Magnetohydrodynamics* **38** 417-422
- [14] Priede J, Buchenau D and Gerbeth G 2006 Contactless electromagnetic induction flowmeter based on phase shift measurements *Proceedings EPM Conference (Sendai, Japan, October 23-27)* 735-740
- [15] Priede J, Gerbeth G, Buchenau D and Eckert S 2008 Verfahren und Anordnung zur kontaklosen Messung des Durchflusses elektrisch leitfähiger Medien *German patent DE 102006018623B4*
- [16] Buceniks I 2000 Perspectives of using rotating permanent magnets for electromagnetic induction pump design *Magnetohydrodynamics* **36** 181-187
- [17] Cramer A, Zhang C and Eckert S 2004 Local flow structures in liquid metals measured by ultrasonic Doppler velocimetry *Flow Meas. Instr.* **15** 145-153
- [18] Eckert S, Gerbeth G and Lielausis O 2000 The behaviour of gas bubbles in a turbulent liquid metal magnetohydrodynamic flow *Int. J. Multiphase Flow* **26** 45-66